LA-UR-18-29656
Approved for public release; distribution is unlimited.

Title: Nanoindentation Characterization of FeCrAl C26M tubes

Author(s): Gigax, Jonathan Gregory
Li, Nan

Intended for: Report

Issued: 2018-10-11

Nanoindentation Characterization of FeCrAl C26M tubes

Fuel Cycle Research & Development

Prepared for
U.S. Department of Energy
Advanced Fuels Campaign

Jonathan G. Gigax
Nan Li

09/28/18

SUMMARY

The present report summarizes the nanoindentation characterization of a FeCrAl alloy, C26M in both tube and bar form. Microstructural analysis on the tube using electron backscatter diffraction showed a textured system with the cross-section favoring orientations near the [110] and the tube surface near the [111]. The bar cross-section showed a texture with orientation favoring those near the [100]. A large amount of in-grain misorientation was observed in the tube specimen with very little in the bar, indicating cold-work from tube processing steps. Nanoindentation with a Berkovich tip measured a similar modulus for all specimens of ~220 GPa. The bar specimens had a hardness of ~3.9 GPa, significantly lower than the 4.8 GPa and 5.2 GPa for the tube cross-section and surface, respectively. Spherical nanoindentation was performed on all specimens and orientations. Indentation with a 100 μm tip resulted in a measured modulus value of ~220 GPa for all specimens, in agreement with the Berkovich indentation results. The nanoindentation yield strength for the bar was found to be ~0.8-0.9 GPa, nearly 0.5 GPa less than the C26M tube.

TABLE OF CONTENTS

FIGURES

TABLES

Intentionally Blank

1. Introduction

FeCrAl alloys are among the most promising "accident tolerant" fuel cladding candidates due to their superior high temperature oxidation resistance, aqueous corrosion resistance, low radiation-induced swelling, and tolerance to loss-of-coolant accident conditions [1-4] . Their higher neutron absorption cross-section requires careful optimization of alloy composition and tube thickness to avoid significantly increasing the enrichment of fuel. However, they possess superior mechanical and thermal properties compared to alternatives (i.e. SiC-based cladding). The ongoing work led by Oak Ridge National Lab has targeted an optimized FeCrAl alloy for tube processing and implementation in light water reactors [5]. Recent characterization of one heat of a FeCrAl alloy, C26M, showed the alloy to have some cold-work that invariably influenced the nanoindentation hardness data [6]. In this study, we perform additional microstructural characterization and nanoindentation analysis on a C26M and C26M bar stock.

2. Materials and Methods

One sample of a C26M tube (Heat #17025001) was obtained and characterized and has a composition given in Table 1. Another sample of bar material (from the plug side of the weld specimen) was taken to compare the impact of tube processing on the microstructure and mechanical response of the C26M. All specimens were ground using successive SiC grit papers down to a grit of 1200. Samples were then polished first using a 0.25 μm diamond solution and finished with a 0.04 μm silica solution.

Table 1. Chemical composition of FeCrAl C26M alloy.

Alloy ID	Fe	Cr	Al	Y	Mo	Si	Nb	C	S	O	N
C26M	bal	11.87	6.22	0.030	1.98	0.2	-	<0.01	0.005	-	-

Scanning electron microscopy of the polished tubes was performed in a FEI Inspect equipped with an EDAX system for acquiring electron backscatter diffraction patterns (EBSD), and obtained with an electron energy of 20 keV. Nanoindentation tests were performed on a Keysight G200 Nanoindenter with a diamond, pyramidal (Berkovich) tip to a final displacement of 2,000 nm with a constant strain rate (loading rate divided by the load) of 0.05 s^{-1}. Continuous stiffness measurements (CSM) were performed at a frequency of 45 Hz and 2 nm displacement amplitude. Hardness and modulus measurements were determined using the Oliver-Pharr method [6]. The tip area function was calibrated by indenting fused silica and using tip properties with a Young's modulus and Poisson's ratio of 1130 GPa and 0.07 (diamond). Spherical nananoindentation tests were performed using two tips with 10 μm and 100 μm radii, respectively. Nanoindentation was performed to a depth of 500 nm using similar system parameters to the nanoindentation with a Berkovich tip. Analysis was performed using a technique outlined by Pathak and Kalidindi [7].

3. Results and Discussion

3.1 Microstructure

Figure 1 shows IPF maps of the two specimens at different orientations. Here, we focus on the tube/bar cross-section and tube/bar surface for analysis. Illustrations of these surfaces and nomenclature are provided as an inset in Fig. 1. Compared to the previous set of tubes examined, Fig. 1a and 1b show that the recent batch of tubing shows a similar texture (orientation near (111)) but with significantly more cold-work. Before being processed into tubing, IPF maps of the C26M bar (Fig. 1c and 1d) show a large degree of texture with most grains on the bar surface oriented near the (100) direction. The grain size in

the C26M tube was found to span a range from 10's μm to 100's μm. The grain size distribution in the C26M bar stock, in comparison, features a similar low-end grain size distribution but does not have many grains larger than 100 μm.

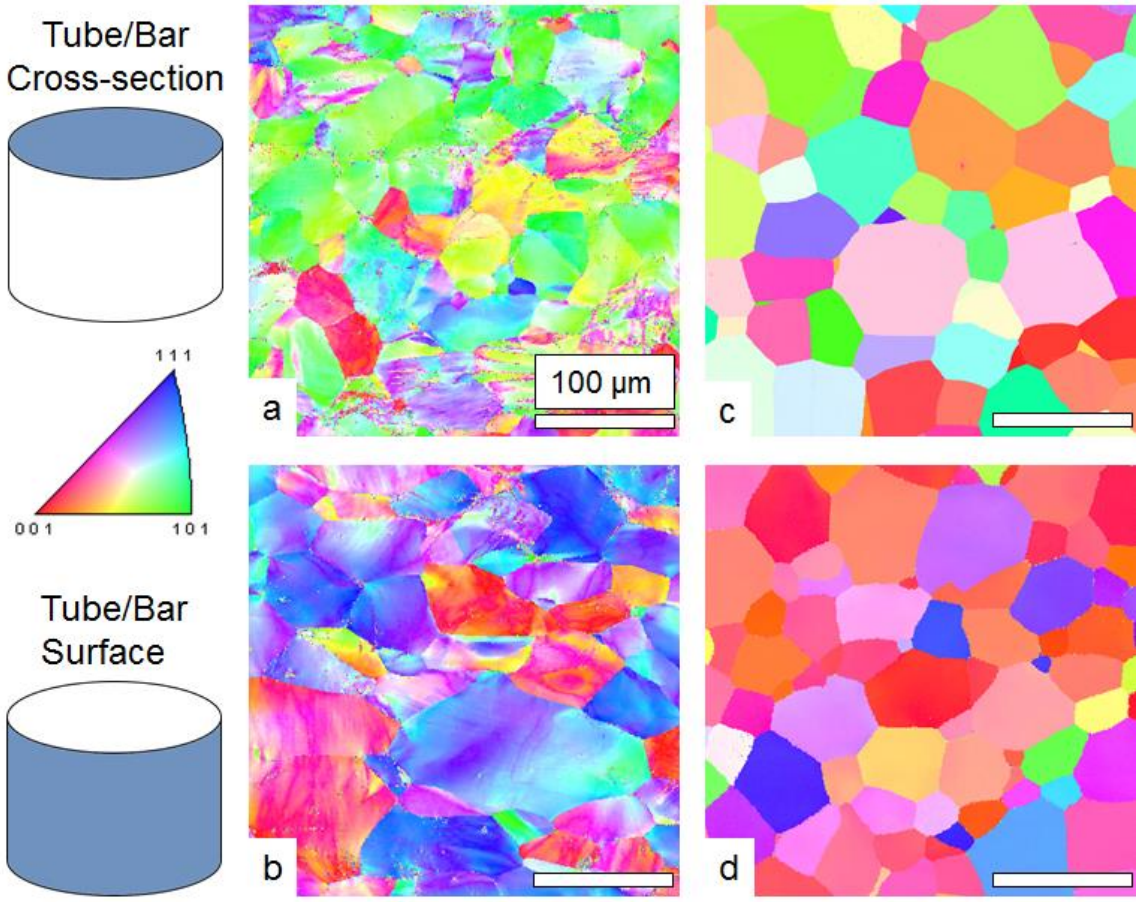

Figure 1 - Inverse pole figure maps for C26M tube (a) cross-section and (b) surface, and C26M bar (c) cross-section and (d) surface. Illustrations of the specimens provided inset on the left-hand side of the figure. Scale bars representing 100 μm on each figure.

Fig. 2 provides a comparison of the grain angle orientation deviation (GROD) maps for both the C26M tube and bar taken from the same region as the IPF maps in Fig. 1. Matching expectation from the IPF maps, the GROD maps for the C26M tube show a significant amount of in-grain misorientation, reaching 20° in many of the grains and up to 60° in some cases. On the other hand, the C26M bar shows very little in-grain misorientation, with only a handful of grains showing a deviation of a few degrees.

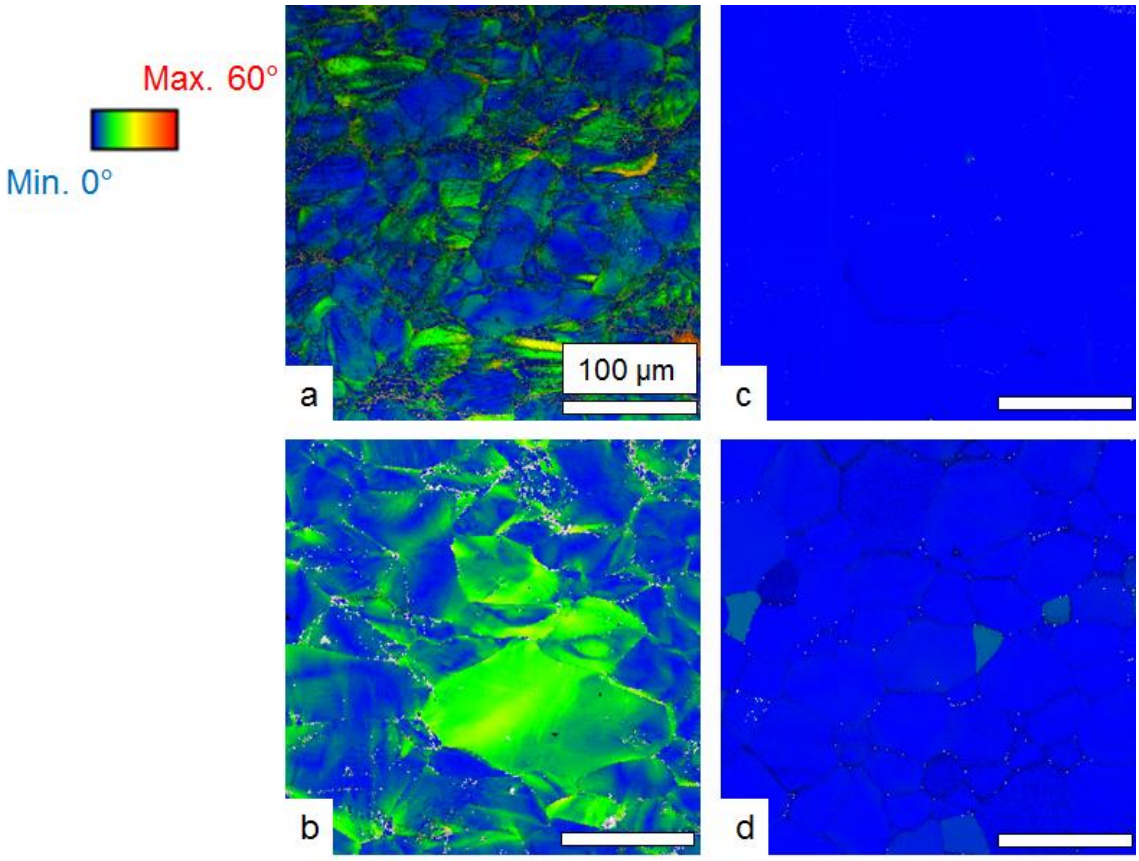

Figure 2 - Grain angle orientation deviation maps for for C26M tube (a) cross-section and (b) surface, and C26M bar (c) cross-section and (d) surface. Scale bars representing 100 µm inset on each figure

3.2 Berkovich Nanoindentation

Figure 3 shows typical nanoindentation modulus and hardness curves as a function of depth for each of the specimens in this study. All samples show a similar modulus value of ~220 GPa. Fig. 3b shows that the hardness of the specimens begins to saturate around 500-600 nm below the surface. To avoid the effects of pile-up at deeper depths, the hardness and modulus of the specimens is averaged between a depth of 400-500 nm and is summarized in Table 2. The nanoindentation hardness of the C26M tube differs by 0.9-1.4 GPa compared to the C26M bar. This difference can be directly attributed to the cold-work introduced from the tube processing and indicated by the EBSD analysis.

It is worth noting that the C26M bar shows no major difference between the two orientations examined, suggesting that the differences in texture may not play a big role in the hardness. In comparison, the C26M tube shows a small but significant difference in hardness between the two orientations. We note that while the tube is more strongly textured than the bar stock and may be one possible explanation of the differences, there is another consideration that must be made.

The indents on the tube cross-section were placed near the center of the tube, while indents on the tube surface were placed on a surface exposed after polishing away ~40-50 µm of material. There is a strong possibility of a greater amount of cold-work from the tube processing in this region compared to that near the center of the tube. For future studies involving ion irradiation or mechanical characterization on the microscale, heat treating the tubes to obtain a more uniform microstructure may be needed.

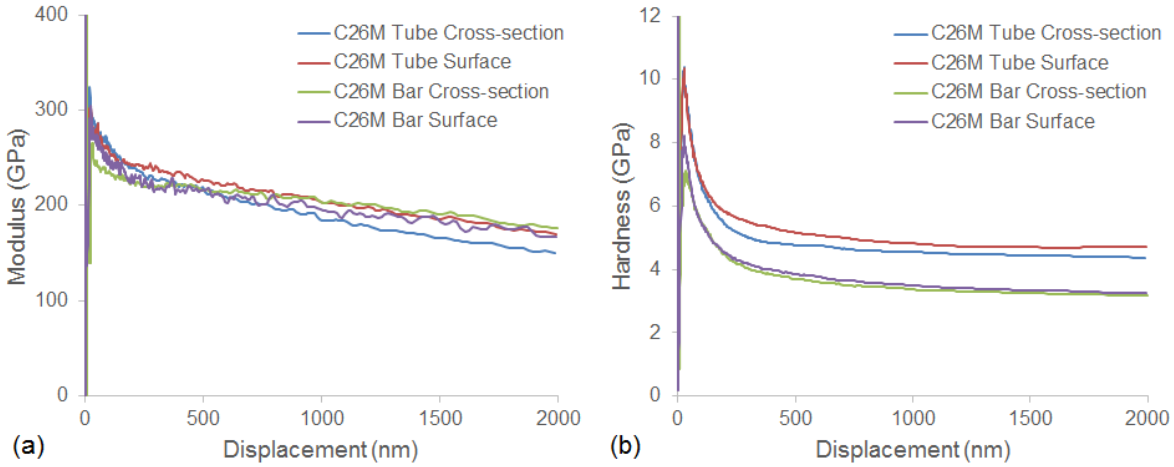

Figure 3 - Nanoindentation (a) modulus and (b) hardness plots as a function of depth for each of the specimens examined in this study.

Table 2. Summary of nanoindentation measurements. Hardness and modulus averages were made over a displacement range of 400-500 nm. Sample averages come from 20-25 tests spaced 75 µm to place indents in multiple grains. The error bars denote one standard deviation.

Specimen	Modulus	Hardness
C26M, Tube Cross-section	222.7 ± 10.7	4.8 ± 0.26
C26M, Tube Surface	229.0 ± 8.4	5.2 ± 0.28
C26M, Bar Cross-section	215.9 ± 6.6	3.8 ± 0.11
C26M, Bar Surface	214.9 ± 7.8	3.9 ± 0.11

3.3 Spherical Nanoindentation

Fig. 4 provides a comparison of typical nanoindentation stress-strain values for each of the specimens examined in this study. Similar to the data from Berkovich nanoindentation, the C26M tube specimens show both a larger yield strength and more strain hardening than the bar counterparts. Specimens were prepared by mechanical polishing with the expectation that a sufficient amount of defects near the surface would be introduced to avoid pop-ins [9]. However, ~35% of the indents on the bar cross-section and more than 50% of the indents on the bar surface exhibited pop-ins. Table 3 provides a summary of the spherical nanoindentation results. All specimens had a similar modulus of ~218 GPa.. However, the tube specimens possessed a nanoindentation yield strength of ~1.4 GPa, nearly 0.5 GPa higher than the C26M bar specimens.

One deviation from the Berkovich nanoindentation was observed with the spherical nanoindentation measurements. From Berkovich indents, the hardness between the two orientations of the C26M tube was small (~0.4 GPa) but significant. With spherical nanoindentation, however, this difference is much smaller (~0.03 GPa). This is thought to arise from the less deterministic method of calculating the yield strength from nanoindentation stress-strain curves. That is, based on the method provided by Pathak and Kalidindi, nanoindentation stress-strain curves are calculated by a processing of fitting the data to *a priori* information about the sample. Enforcing strong error metrics typically results in several thousand good fits of the stress-strain curve whose yield strength can vary a few hundred MPa. To avoid bias in selecting representative stress-strain curves, we average all viable fits from a single spherical indent into a single curve. Although this method is more objective, as the yield strength is not assumed to be known,

this process tends to reduce the differences between indents, resulting in less sensitivity to small changes in the microstructure.

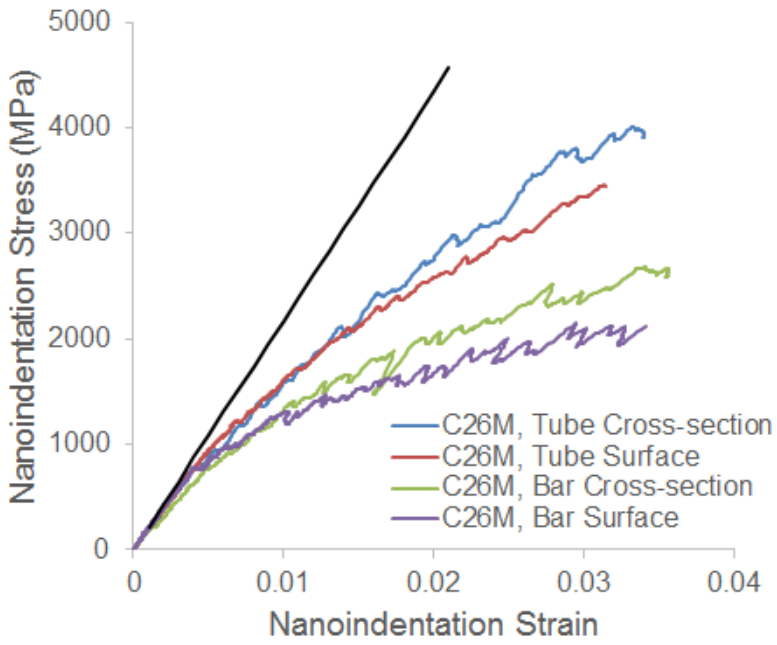

Figure 4 - Typical nanoindentation stress-strain curves of each specimen in this study. A solid black line with a slope equal to the modulus is provided for reference.

Table 3. Summary of nanoindentation modulus and nanoindentation yield strength obtained from spherical indentation with a 100 µm tip.

Specimen	Modulus (GPa)	Yield Strength (MPa)
C26M, Tube Cross-section	217.8 ± 0.73	1369.4 ± 103.6
C26M, Tube Surface	217.6 ± 1.1	1399.9 ± 76.4
C26M, Bar Cross-section	218.4 ± 2.5	885.0 ± 141
C26M, Bar Surface	215.9 ± 6.2	936.0 ± 205.3

In order to facilitate the yield strength comparison obtained from spherical nanoindentation to those from macroscale tests, finite element simulations on an isotropic material have shown that the uniaxial and nanoindentation stress states can be related by [9],

$$\sigma = \frac{\sigma_{ind}}{2.2}$$

Where σ_{ind} is the nanoindentation stress state and σ is the uniaxial stress state. Applying this conversion to the data in Table 3 more closely matches the results obtained from macroscale tensile tests.

4. Conclusions and Future Work

In this study, we have performed characterization of the microstructure of C26M in both tube and bar form. Nanoindentation with a Berkovich tip was utilized to evaluate the hardness of the cross-section and tube surface of both C26M forms. The tube specimens show dramatically higher hardness (4.8-5.2 GPa) than the bar counterparts (~3.9 GPa) with a slight difference between orientations in the tube. This difference was attributed to the fact that the indents on the tube cross-section were placed near the center of the tube wall while the indents on the tube surface were only ~50 μm below the outer surface of the tube.

Spherical nanoindentation was also performed using a large 100 μm spherical tip to avoid pop-in issues. For all specimens, the modulus measured by spherical nanoindentation was ~220 GPa, in agreement with the berkovich measurements. Despite the large number of pop-ins observed in different indents in the C26M bar, the nanoindentation yield strength was measured to be 0.88 and 0.94 GPa for the cross-section and surface, respectively. This was nearly 0.5 GPa lower than the yield strength measured for the C26M tube, similar to the hardness data.

The differences between the tube and bar, and between the tube orientations suggests that some form of tube annealing will be required for more systematic studies. For a comparison of mechanical property changes after ion irradiation to previous FeCrAl alloys or other systems, or even with different tubes of the same heat, a baseline with little cold-work is needed.

5. References

1. R.B. Rebak, K.A. Terrani, W.P. Gassmann, J.B. Williams, K.L. Ledford. Improving Nuclear Power Plant Safety with FeCrAl Alloy Fuel Cladding, MRS Advances (2017) 1-8.
2. Y. Yamamoto, B.A. Pint, K.A. Terrani, K.G. Field, Y. Yang, L.L. Snead. Development and property evaluation of nuclear grade wrought FeCrAl fuel cladding for light water reactors, J Nucl Mater 467, Part 2 (2015) 703-716.
3. K.G. Field, M.N. Gussev, Y. Yamamoto, L.L. Snead. Deformation behavior of laser welds in high temperature oxidation resistant Fe–Cr–Al alloys for fuel cladding applications, J Nucl Mater 454 (2014) 352-358.
4. S.J. Zinkle, K.A. Terrani, L.L. Snead. Motivation for utilizing new high-performance advanced materials in nuclear energy systems, Current Opinion in Solid State and Materials Science 20 (2016) 401-410.
5. Y. Yamamoto, Z. Sun, B.A. Pint, K.A. Terrani. Optimized Gen-II FeCrAl cladding production in large quantity for campaign testing. Oak Ridge: Oak Ridge National Laboratory, 2016.
6. J. Gigax, J. S. Weaver, and N. Li. Microstructural Characterization of FeCrAl C26M Tubes. Los Alamos, NM: Los Alamos National Lab, 2017.
7. W.C. Oliver, G.M. Pharr. Measurement of hardness and elastic modulus by instrumented indentation: Advances in understanding and refinements to methodology, J Mater Res 19 (2004) 3-20.
8. S. Pathak, S. R. Kalidindi. Spherical nanoindentation stress-strain curves. Mater. Sci. Eng. R 91 (2015) 1-36.
9. Z. Wang, H. Bei, E. P. George, G. M. Pharr. Influences of surface preparation on nanoindentation pop-in in single-crystal Mo. Scripta Mater. 65 (2011) 469-472.
10. D.K. Patel, S.R. Kalidindi. Correlation of spherical nanoindentation stress-strain curves to simple compression stress-strain curves for elastic-plastic isotropic materials using finite element models. Acta Mater. 112 (2016) 295-302.